Journal of Membrane Science 661 (2022) 120915

Contents lists available at ScienceDirect

Journal of Membrane Science

journal homepage: www.elsevier.com/locate/memsci

Oxidative coupling of methane (OCM) conversion into C_2 products through a CO_2/O_2 co-transport membrane reactor

Kangkang Zhang, Shichen Sun, Kevin Huang *

Department of Mechanical Engineering, University of South Carolina, Columbia, SC, 29201, USA

ARTICLE INFO

Keywords:
Membrane reactor
Flue gas
Methane
Ethane
Ethylene

ABSTRACT

Oxidative coupling of methane (OCM), which transforms CH_4 into C_2 products (C_2H_6 and C_2H_4) with molecular O_2 as the oxidant, is one of the most studied direct methane conversions (DMCs). However, a major technical hurdle to the OCM process is to achieve high CH_4 conversion at high C_2 (C_2H_6 and C_2H_4) selectivity. One rudimentary cause for this "tradeoff" behavior is the high chemical reactivity of the products (C_2H_6 or C_2H_4), which can be re-oxidized by O_2. To overcome this thermodynamic challenge, minimizing the oxidizing power of the oxidant and lowering the local oxygen partial pressure are keys. In this work, we demonstrate a new membrane reactor that capture CO_2/O_2 from a flue gas and uses it for OCM conversion. The results show that the co-captured CO_2/O_2 mixture converts CH_4 into C_2H_6 in the presence of a 2%Mn–5%Na_2WO_4/SiO_2 catalyst, followed by thermal cracking of C_2H_6 into C_2H_4 and H_2. The presence of CO_2 decreases the local partial pressure of O_2, thus reducing the propensity of C_2-products re-oxidation and leading to a higher C_2 selectivity. We show that a small button-type membrane reactor can achieve 12% C_2 yield with ~57% C_2-selectivity using a diluted CH_4-Ar mixture as the feedstock. We expect higher C_2 yield with tubular plug-flow membrane reactors in the future. We also highlight the unique advantage of the membrane reactor in intensifying CO_2 capture from both flue gas and OCM purification process into one single step.

1. Introduction

In recent decades, climate change has been increasingly observed to disrupt our daily lives and harm our economy. Scientific evidence has linked it to human activities such as burning of fossil fuels, a process which emits large quantities of CO_2 (a greenhouse gas), into the atmosphere. The virtually unlimited release of CO_2 in the past has led to a >40% increase in atmospheric CO_2 concentration and a net ~1 °C rise in the Earth surface temperature since the Industrial Revolution [1]. Therefore, to fundamentally address global warming and climate change problems, mitigating the release of CO_2 into the atmosphere is imperative. The current best and realistic practice to curb CO_2 emissions is to capture it at major point-sources, such as coal-fired power plants, and geologically store it underground for enhanced oil recovery (EOR) [2]. However, today's carbon capture technologies (carbon capture and storage or collectively CCS) are still too expensive and energy intensive to implement [3,4]. Such CCS implementation into existing or new fossil-fuel power plants would drastically lower the plant efficiency and increase the cost of electricity. Developing more efficient and cost-effective CO_2 capture technologies is, therefore, highly desirable.

Using membranes to separate CO_2 from a flue gas stream presents advantages in cost, energy consumption and operation [5]. Many types of membranes have so far been demonstrated for CO_2 capture, examples of which include porous inorganics and polymers operated on the principles of size-exclusion and dissolution-diffusion. However, the instability in humid and hot environments has prevented them from scaling up [6,7]. An ongoing effort to tackle these problems is to develop high-temperature CO_2 transport membrane (CTMs) [8], which has a potential to achieve lower cost and higher efficiency since the heat in hot flue gas can be directly utilized.

A leading class of high temperature multiphase CTMs is operated on ion/electron-transport electrochemistry. Based on the types of charge carriers, they can be principally grouped into two categories: (1) mixed electronic and carbonate-ionic conductor (MECC) membrane and (2) mixed oxide-ionic and carbonate-ionic conductor (MOCC) membrane. MECC membranes typically use metal as the matrix into which molten carbonate (MC) is retained. In comparison, MOCC membranes use oxide-ion conducting ceramics as the matrix [9,10]. Fig. 1 shows the

* Corresponding author.
E-mail address: huang46@cec.sc.edu (K. Huang).

https://doi.org/10.1016/j.memsci.2022.120915
Received 27 June 2022; Received in revised form 4 August 2022; Accepted 9 August 2022
Available online 16 August 2022
0376-7388/© 2022 Elsevier B.V. All rights reserved.

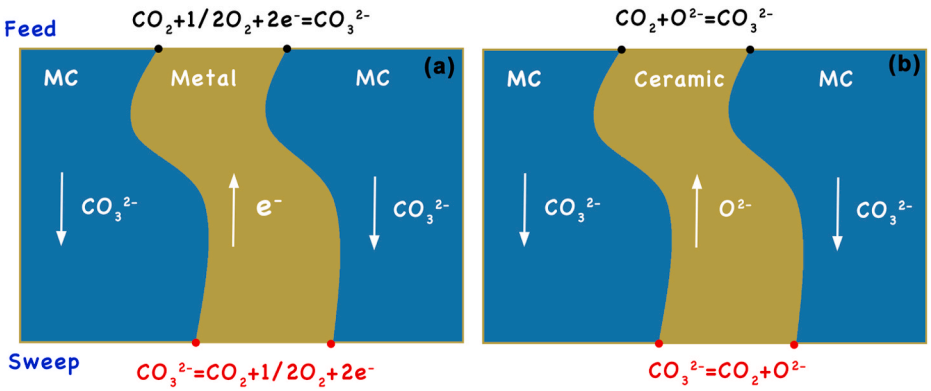

Fig. 1. Schematic of CTM transport mechanisms: (a) MECC; (b) MOCC.

configuration and ion/electron-transport enabling surface reactions of the two membranes.

In common, the CO_2 transports through these two types of membranes are achieved in the form of CO_3^{2-}, of which ionic transport is realized by MC phase. The difference between these two CTMs mainly lies in the charge-balancing counter ions. For MECC membranes (see Fig. 1a), the CO_3^{2-} is formed by the reaction between CO_2, O_2 and electrons (e^-) (from the metal phase) on the feed side (the top) of the membrane, after which CO_3^{2-} is transported under the chemical potential of CO_2 to the sweep side (the bottom) of the membrane, where pure CO_2 and O_2 are released to a sweeping gas with an exact flux ratio of 2:1. As a balancing charge carrier, e^- flows in the opposite direction of CO_3^{2-} in the metal phase. Similarly, CO_3^{2-} transport in MOCC membranes can be charge-compensated by O^{2-} in the oxide-ion conducting phase, see Fig. 1b. The CO_3^{2-} is formed via the reaction between CO_2 and O^{2-} on the feed side, transported through the MC phase and dissociated into CO_2 at the sweep side of membrane. According to the CO_2 transport chemistry of these two types of membranes, MECC membranes are more suited for CO_2 capture from an oxidizing stream, such as post combustion flue gas, while MOCC membranes are more adequate for CO_2 separation from a CO_2-rich gas, for example, a mixture of CO_2 and H_2 in the pre-combustion process [11].

Another recent notable development in the energy field is the significantly increased production of natural gas (NG) from shale and tight oil [12,13]. If such newly available, low-cost NG is used primarily for producing heat and power as in the past, CO_2 will continue to be pumped into the atmosphere and further burden current efforts to capture CO_2 [14]. Over the last several decades, extensive studies have focused on direct methane conversion (DMC) into value-added products such as ethane (C_2H_6) and ethylene (C_2H_4), two of the largest commodities and the vital building block for a wide range of chemicals [15–17]. Moreover, the DMC approach is economically attractive due to the large price differential between NG and the final products (e.g. C_2H_4). However, the ethane and ethylene formed by oxidative coupling of methane (OCM) tend to be re-oxidized by O_2, which significantly decrease the C_2-selectivity [18–20]. For example, Ortiz-Bravo et al. [19] assembled CH_4 and O_2 co-fed reactor with different catalysts to study the performance of OCM. The results show the best C_2 selectivity <50% at 800 °C. To improve C_2-selectivity, oxygen transport membranes (OTMs) have been considered over conventional co-fed reactor as a means of mixing O_2 with CH_4 in a controlled way (e.g. along the length of membrane surface) to minimize re-oxidation of C_2-products [21–23]. For example, Czuprat et al. [21] demonstrated OCM performance with maximum 17% C_2 yield and 50% C_2 selectivity at 800 °C using a $BaCo_xFe_yZr_z$-based OTM. With a membrane microreactor using $La_{0.6}Sr_{0.4}Co_{0.2}Fe_{0.8}O_{3-\delta}$ (LSCF) hollow fiber as an OTM and *in-situ* deposition of $Bi_{1.5}Y_{0.3}Sm_{0.2}O_{3-\delta}$ (BYS) as catalyst, Othman et al. [22] showed a high 39% C_2 yield and 79% C_2 selectivity at 900 °C. However, many good OTM materials are based on Ba/Sr-containing perovskites that are chemically unstable in high CO_2-containing atmospheres at high temperatures, forming OCM-blocking carbonates and thus limiting their potential applications [24–26].

We herein report on a high-temperature, chemically stable CTM for OCM conversion to C_2 products. It is based on MECC membrane chemistry, by which the CO_2 and O_2 are co-captured from a flue gas, a major source of CO_2 emissions on the earth. Upon arriving at the CH_4-side across the membrane, the transported O_2 (diluted by CO_2) reacts with CH_4 to form C_2H_6 and C_2H_4 via OCM reactions in the presence of suitable catalysts. The configurations of such a CTM-based OCM reactor are schematically shown in Fig. 2.

As many co-fed OCM reactor systems, if commercially implemented, will require downstream ethylene purification process from a mixture of

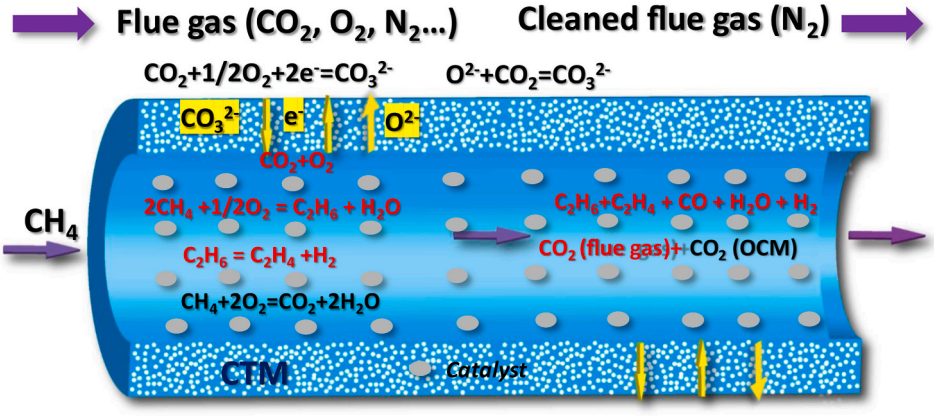

Fig. 2. Working principle of the CTM-based OCM reactor.

Table 1
The porosity (ε) and tortuosity (τ) and average radius of pores (*r*) of porous SDC-NiO matrix sintered at 1150 °C.

Sample	ε	τ	*r (nm)*
SDC-NiO	0.35	1.63	99

CO_2, C_2H_6, C_2H_4, H_2O, H_2 and CO, one distinct advantage of CTM-based OCM reactors is that it combines CO_2 captured from flue gas with that produced in the OCM process into one stream for capture, thus significantly reducing cost and saving energy. We have previously shown computationally the advantages of using CO_2/O_2 co-transport membrane reactor for the OCM conversion [27], but no experimental studies have been performed so far.

Here in this work, we use an MECC-based CTM comprising of SDC ($Sm_{0.2}Ce_{0.8}O_{1.9}$), NiO, and MC phases for demonstration of the OCM performance with a mockup flue gas as a feedstock and a 2%wt. Mn-5% wt.Na_2WO_4/SiO_2 catalyst in a temperature range of 775–850 °C. We also assess the co-CO_2/O_2 transport mechanisms, main/side reactions occurring in the OCM process and long-term stability of the OCM conversion.

2. Experimental procedures

2.1. Preparation of membrane and catalyst

The SDC and NiO composite powers were prepared via co-precipitation method. Stoichiometric amounts of starting materials, Ni $(NO_3)_2{\cdot}6H_2O$ (Alfa Aesar, 99%), $Sm(NO_3)_2{\cdot}6H_2O$ (Alfa Aesar, 99%) and $Ce(NO_3)\cdot6H_2O$, were first dissolved into deionized (DI) water. Then the obtained solution was slowly added into a $(NH_4)_2CO_3$ (Fisher Scientific, Atlanta, 95%) solution. The volumetric ratio of these two solutions is controlled to have a carbonate anions/total metallic cations ratio of 2.5 (on a molar basis). After co-precipitation, the precipitate was first filtered, and then dried at 80 °C overnight, followed by firing at 650 °C for 4 h to obtain the final SDC-NiO powders. The volume ratio of NiO and SDC in the precipitate is controlled to be 50:50. The obtained SDC-NiO powders were then blended with 20 wt% carbon as pore former, ball-milled for 3 h. After mixing and drying, the powder mixture was pelletized under ~100 MPa and subsequently sintered at 1150 °C in air for 4 h. The high-temperature firing the sample in oxidizing atmosphere burns out carbon, leaving behind a porous SDC-NiO pellet. The final dimension and porosity of the resultant SDC-NiO pellets are ~14 mm in diameter and 0.7 mm in thickness and 35%, respectively.

A binary eutectic MC phase (Li_2CO_3:Na_2CO_3 = 52:48 mol%) was infiltrated *in situ* into the porous SDC-NiO pellets to form the final dense SDC-NiO-MC membrane. To investigate the chemical stability between SDC-NiO and MC, we blended SDC-NiO with MC powders (SDC:NiO:MC = 1:1:3 in volume) and fired at 850 °C for 2 h.

The catalyst 2 wt%Mn-5wt.%Na_2WO_4/SiO_2 was prepared via incipient-wetness impregnation method, and the details can be found in previous work [28]. The XRD pattern, particle size and BET surface area of the catalyst are given in Fig. S1 and Table 1, respectively.

2.2. Characterization of porous SDC-NiO matrix and SDC-NiO-MC membrane

The as-synthesized SDC-NiO, SDC-NiO-MC and 2%Mn–5%Na_2WO_4/SiO_2 powders were examined with X-ray diffraction (XRD, Rigaku D/MAX-2100) for phase identification and with Micromeritics ASAP2020 adsorption analyzer for BET surface area. The microstructure of SDC-NiO pellets and SDC-NiO-MC membrane were analyzed by a scanning electron microscope (SEM, Zessis Ultra plus) coupled with an energy dispersive spectroscopy (EDS). Relative densities of the sintered porous SDC-NiO pellets were determined by the Archimedes' method. Room temperature helium permeation test was also used to measure the tortuosity and average pore size of the porous SDC-NiO support. The details on the procedure can be found in our previous work [10].

2.3. CO_2/O_2 flux measurement of SDC-NiO-MC membrane

The testing procedure of the membrane performance was followed the same as that previously described [10,29]. The feed gas was the mockup flue gas of 75 mL min^{-1} N_2, 15 mL min^{-1} CO_2 and 10 mL min^{-1} O_2, while a high-purity Ar at a flow of 50 mL min^{-1} was fed to the other side as the sweep gas. The presence of N_2 in feed gas was also used for leakage correction. The compositions of sweep gas were analyzed by an on-line GC (Agilent Micro 490-GC). The membrane was first heated to 850 °C at a rate of 2 °C/min and held for 1 h to ensure equilibrium between MC and SDC-NiO matrix. The GC data were collected from 850 to 650 °C and roughly 60 min were given at each temperature to ensure full equilibrium.

The flux densities of the CO_2 and O_2 are calculated by:

$$J_{CO_2} = \frac{C_{CO_2}}{1 - C_{CO_2} - C_{O_2} - C_{N_2}} \times \frac{Q}{S} \quad (1)$$

$$J_{O_2} = \frac{C_{O_2}}{1 - C_{CO_2} - C_{O_2} - C_{N_2}} \times \frac{Q}{S} \quad (2)$$

where Q is the mass flow rate of Ar sweeping gas; S is the effective area of the membrane, 0.921 cm^2 for this work; C_{CO_2}, C_{O_2} and C_{N_2} are the measured concentration of CO_2, O_2, and N_2 respectively. The concentration of N_2 was found very low (<0.1%) for all measurements, suggesting a well-sealed permeation cell and accuracy of the collected data.

2.4. Performance measurements of CTM-based OCM reactor

For CTM-based OCM reactor performance evaluation, the feed gas was kept the same: 75 mL min^{-1} N_2, 15 mL min^{-1} CO_2 and 10 mL min^{-1} O_2, while the sweep gas was switched from a pure Ar to mixture of CH_4 and Ar with a CH_4 concentration varying from 2.5 to 10%. Roughly 0.05 g of catalysts was spread over an alumina wool and loaded into the sweep-gas chamber right beneath the membrane. The distance between catalyst bed and membrane surface was kept approximately 1 mm. The operating temperature of OCM experiment was varied from 775 to 850 °C. The concentrations of CO_2, CH_4, C_2H_6, C_2H_4, H_2, and N_2 in the effluent were analyzed by an on-line GC (Agilent Micro 490-GC). The data collection procedures are same as described above. The conversion of CH_4 (X_{CH_4}) are calculated by:

$$X_{CH_4}(\%) = \frac{F_{CH_4}(in) - F_{CH_4}(out)}{F_{CH_4}(in)} \times 100\% \quad (3)$$

where $F_{CH_4}(in)$ and $F_{CH_4}(out)$ are the mass flow rates (mL·min^{-1}) of CH_4 into and out of the reactor, respectively.

The flux density (mL·min^{-1}·cm^{-2}) of CO_2, CH_4, C_2H_6, C_2H_4, H_2, and N_2 in the effluent are calculated by:

$$J_{CO_2} = \frac{C_{CO_2}}{1 - C_{CO_2} - C_{CH_4} - C_{C_2H_6} - C_{C_2H_4} - C_{H_2} - C_{N_2}} \times \frac{F_{Ar}}{S} \quad (4)$$

$$J_{CH_4} = \frac{C_{CH_4}}{1 - C_{CO_2} - C_{CH_4} - C_{C_2H_6} - C_{C_2H_4} - C_{H_2} - C_{N_2}} \times \frac{F_{Ar}}{S} \quad (5)$$

$$J_{C_2H_6} = \frac{C_{C_2H_6}}{1 - C_{CO_2} - C_{CH_4} - C_{C_2H_6} - C_{C_2H_4} - C_{H_2} - C_{N_2}} \times \frac{F_{Ar}}{S} \quad (6)$$

$$J_{C_2H_4} = \frac{C_{C_2H_4}}{1 - C_{CO_2} - C_{CH_4} - C_{C_2H_6} - C_{C_2H_4} - C_{H_2} - C_{N_2}} \times \frac{F_{Ar}}{S} \quad (7)$$

$$J_{H_2} = \frac{C_{H_2}}{1 - C_{CO_2} - C_{CH_4} - C_{C_2H_6} - C_{C_2H_4} - C_{H_2} - C_{N_2}} \times \frac{F_{Ar}}{S} \quad (8)$$

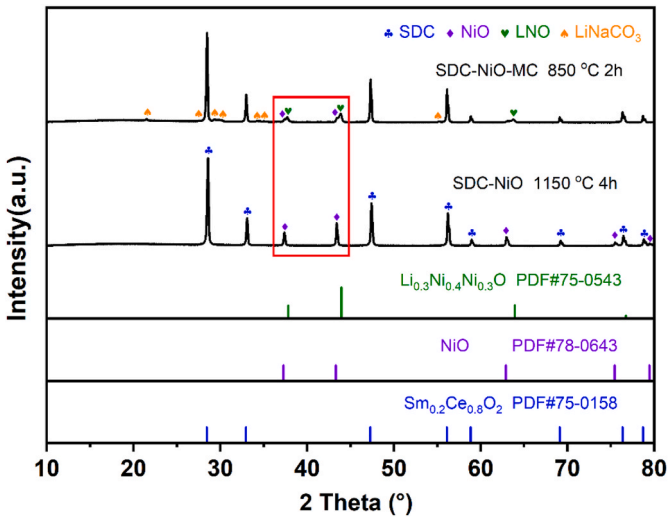

Fig. 3. XRD patterns of SDC-NiO matrix after sintering at 1150 °C and SDC-NiO-MC mixture (volume ratio of SDC:NiO:MC = 1:1:3) after firing at 850 °C.

where C_{CO_2}, C_{CH_4}, $C_{C_2H_6}$, $C_{C_2H_4}$, C_{H_2}, and C_{N_2}, are the measured concentrations of CO_2, CH_4, C_2H_6, C_2H_4, H_2, and N_2, respectively, in the effluent; F_{Ar} is the flow rate of Ar in the sweep gas.

The C_2 products selectivity (S_{C_2}) and yield (Y_{C_2}) are calculated by:

$$S_{C_2}(\%) = \frac{2 \times \left(J_{C_2H_6} + J_{C_2H_4}\right) \times S}{F_{CH_4}(in) - F_{CH_4}(out)} \times 100\% \quad (9)$$

$$Y_{C_2}(\%) = S_{C_2} \times X_{CH_4} \times 100\% \quad (10)$$

3. Results and discussion

3.1. Phase and microstructural properties of the membrane

Fig. 3 shows the XRD patterns of SDC-NiO matrix after sintering at 1150 °C for 4 h; only the peaks corresponding to SDC and NiO are present, indicating that no chemical reaction between SDC and NiO during the sintering. The XRD patterns of SDC-NiO-MC mixture (volume ratio of SDC:NiO:MC = 1:1:3) fired at 850 °C for 2 h are also shown in Fig. 3. It is evident that with the addition of MC into SDC-NiO, a new electron-conducting phase $Li_{0.3}Ni_{0.4}Ni_{0.3}O$ (or $Li_{0.6}Ni_{1.4}O_2$, LNO) is formed, accompanying with apparently decreased amount of NiO phase (see red rectangle). The formed electron-conducting LNO phase is

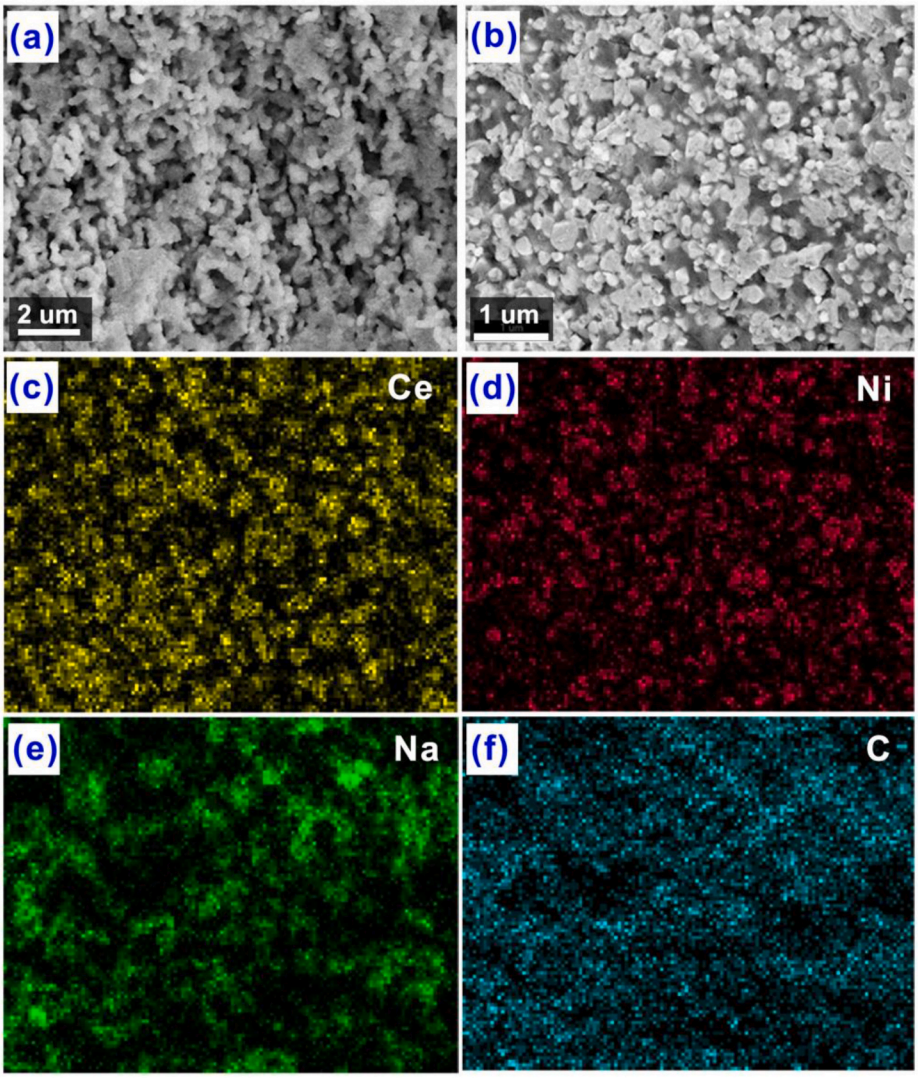

Fig. 4. Cross-sectional views of microstructure of SDC-NiO porous matrix after sintering at 1150 °C (a), and SDC-NiO-MC membranes (b) with elemental mapping of Ce (c), Ni (d), Na (e), and C (f).

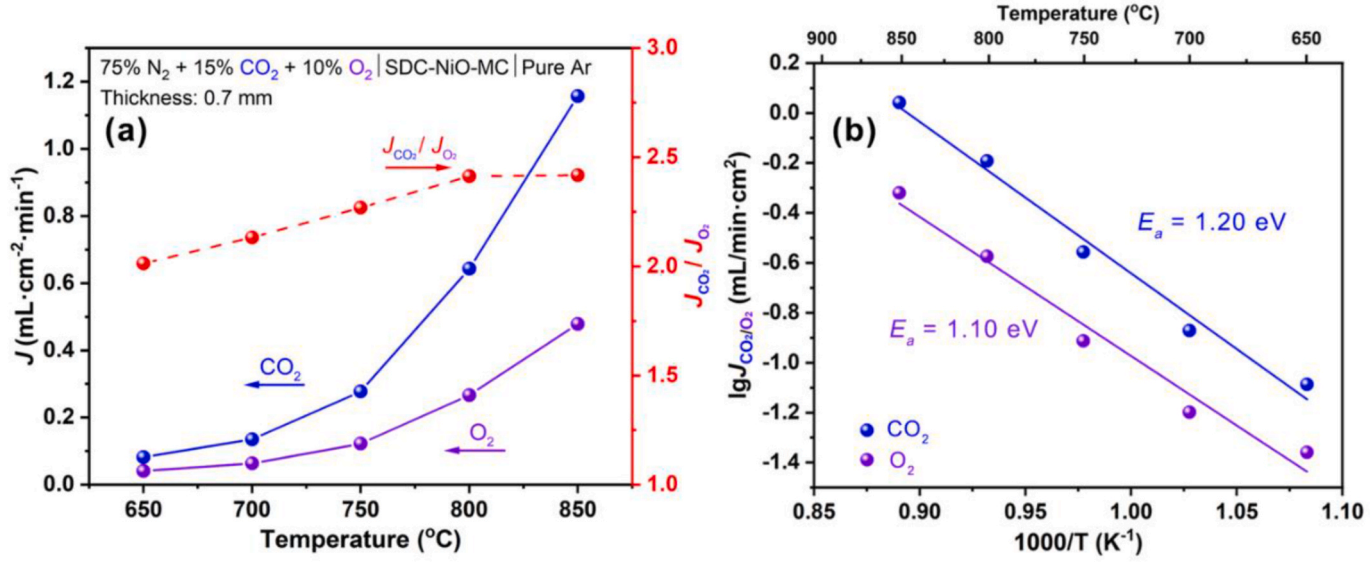

Fig. 5. Temperature dependence of CO_2/O_2 flux densities of SDC-NiO-MC membrane (a) and the corresponding Arrhenius plots (b).

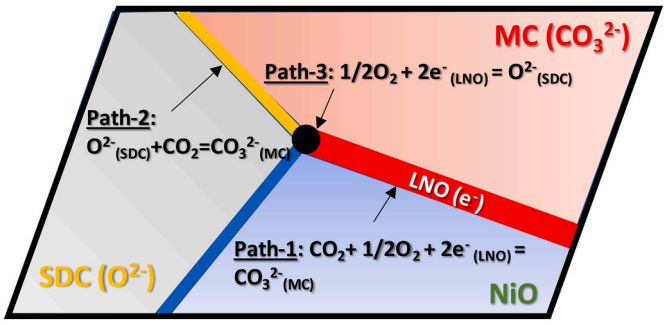

Fig. 6. Schematic of three possible parallel pathways for CO_2/O_2 co-transport in SDC-NiO-MC membrane (feed-side only); lines and points represent multi-phase boundaries (MPBs).

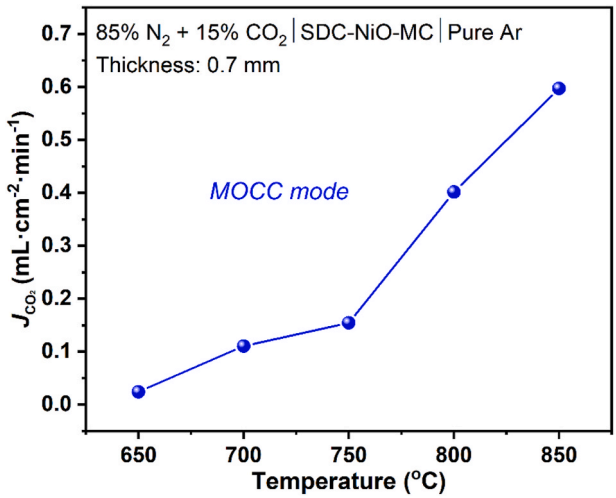

Fig. 7. Temperature dependence of CO_2 flux density of SDC-NiO-MC membrane through MOCC mode.

resulted from the reaction between NiO and MC, as suggested by our previous study [29,30]. Overall, Fig. 3 shows that the chemical compatibility between SDC and NiO and between SDC and MC are both excellent. The MC phase is not obvious from the XRD pattern due to its amorphous nature.

The cross-sectional views of porous SDC-NiO matrix and SDC-NiO-MC membrane are shown in Fig. 4. Clearly, the SDC-NiO support has well-interconnected and evenly distributed pores (Fig. 4a). Corresponding to this microstructure, Table 1 shows the measured the porosity (ε), tortuosity (τ) and average radius of pores (*r*) of the porous SDC-NiO matrix.

3.2. Basic CO_2/O_2 permeation properties of the membrane

After impregnation of MC, Fig. 4b shows that all pores in the porous SDC-NiO matrix are filled, resulting in a dense microstructure, which ensures the permeated CO_2/O_2 are both resulted from concomitant transport of $CO_3^{2-}/e^-/O^{2-}$ rather than from physical leakage. The corresponding elemental mapping in Fig. 4c–f also confirms that SDC-NiO and MC phases are intimately mixed and evenly distributed in the membrane, suggesting good wettability between the solid and liquid phases.

The temperature-dependent CO_2/O_2 flux densities of SDC-NiO-MC membrane with a mockup flue gas (75% N_2 + 15% CO_2 + 10% O_2) as feeding gas and Ar as the sweep gas are shown in Fig. 5a. The increase of CO_2/O_2 flux density with temperature suggests that CO_2/O_2 transport through the membrane is a thermally activated process. On the other hand, the flux ratio of CO_2/O_2 is found to be in the range of 2.01–2.42 from 650 to 850 °C, which apparently deviates from the theoretical 2:1 ratio of MECC membranes, implying additional CO_2 transport pathway in the membranes. The close activation energy for CO_2 and O_2 transport, *i.e.* 1.20 *vs.* 1.10 eV, shown in Fig. 5b supports the co-CO_2/O_2 transport mechanisms.

To understand the multiple ion/electron transport pathways, we sketch Fig. 6 to show all the available multi-phase boundaries (MPBs), where possible parallel enabling surface reactions are illustrated to take place within the SDC-NiO-MC membrane. Note that MC and SDC are pure CO_3^{2-} and O^{2-} ionic conductors, respectively, while LNO formed *in situ* between MC and NiO phase at high temperatures (see Fig. 3), is the electronically conducting phase. There are three possible pathways identified for CO_2/O_2 transport across the SDC-NiO-MC membrane: path-1, 2, 3 are based on MECC, MOCC and OTM pathways, respectively. Since some O_2 is contained in flue gas, it will activate the MECC mode (path-1), where both CO_2 and O_2 permeate to the sweep side, as evidenced by Fig. 5a.

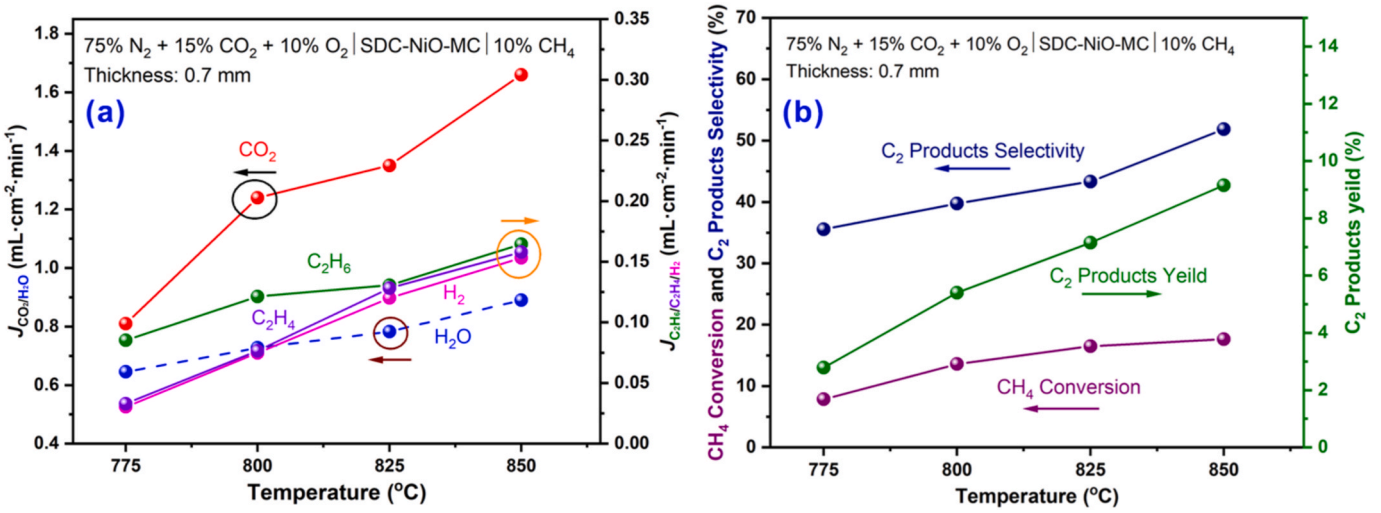

Fig. 8. OCM performance of SDC-NiO-MC membrane under 10% CH_4 as sweep gas. Effect of temperature on flux of C_2H_6, C_2H_4, H_2 and CO_2 (a), and CH_4 conversion, C_2 products selectivity and yield (b).

To prove the MOCC pathway (path-2), the O_2 in mockup flue gas is purposely shut down. The results shown in Fig. 7 indicate a significant level of CO_2 is still detected in the sweep gas. This observation suggests the active MOCC pathway, *i.e.* $CO_2+O^{2-}=CO_3^{2-}$. However, when CO_2 in the mockup flue gas is cut off, *i.e.* feed gas becoming 90% N_2 + 10% O_2, neither CO_2 nor O_2 is detectable in the sweep gas. This observation implies that the OTM-pathway (path-3) is inactive. This is understandable in that the density of the path-3 is very low due to the nature of *in-situ* formation of electron-conducting LNO phase, see Fig. 6. It is also not guaranteed that path-3 forms effective percolation to sustain oxygen permeation. In addition, the partial pressure of O_2 in the feed gas (10%) is rather low, which is unfavorable to permeate sufficient O_2 to be detected by GC. Overall, the CO_2 transport primarily follows path-1, yielding CO_2:O_2 = 2:1 (see Fig. 1a) and the secondary CO_2 pathway is path-2, yielding pure CO_2 (see Fig. 1b), which ultimately results in a CO_2/O_2 flux ratio >2:1, see Fig. 5a.

3.3. OCM performance of the membrane

After understanding the basic transport mechanisms with pure Ar as the sweep gas, the membrane's OCM performance was further evaluated *vs.* temperature using 10%CH_4-Ar as the sweep gas; the results are shown in Fig. 8. Clearly, C_2H_6, C_2H_4, H_2, CO_2 and H_2O are the main products in the effluent. Note that H_2O flux density is calculated using H-mass balance due to its undetectability by GC. As the temperature increases, see Fig. 8a, the flux densities of all gaseous species all increase correspondingly.

To understand the detected species and their concentrations, we analyze the following main and side reactions to account for OCM conversion:

$$2CH_4 + 0.5O_2 = C_2H_6 + H_2O \quad (11)$$

$$C_2H_6 = C_2H_4 + H_2 \quad (12)$$

$$2CH_4 + O_2 = C_2H_4 + 2H_2O \quad (13)$$

$$CH_4 + 2O_2 = CO_2 + 2H_2O \quad (14)$$

$$C_2H_6 + 3.5O_2 = 2CO_2 + 3H_2O \quad (15)$$

$$C_2H_4 + 3O_2 = 2CO_2 + 2H_2O \quad (16)$$

The fact that the flux densities of C_2H_4 and C_2H_6 are slightly higher than H_2 suggests that the main reactions for C_2-product (C_2H_4 and C_2H_6) are (11) and (12); reaction (13) is very limited, with the catalyst we used. The large amount of CO_2 remained in the effluent also suggests the inactive role of CO_2 in forming C_2-product and likelihood of side reactions of (14), (15) and (16). The CH_4 conversion and C_2 selectivity all increase with temperature, see Fig. 8b, which is understandable because the fluxes of permeated O_2 and CO_2 also increase with temperature (see Fig. 5a), thus increasing the rate of O_2–CH_4 reaction to form C_2H_6 as well as subsequent thermal cracking into C_2H_4 and H_2. Meanwhile, the permeate CO_2 could potentially suppress the direct methane oxidation (reaction (14)) and re-oxidation of C_2H_6 and C_2H_4 (reaction (15) and (16)), thus helping C_2-selectivity. On top of the above, the decreased local O_2 partial pressure alleviates the direct oxidation of CH_4 and re-oxidation of C_2H_6 and C_2H_4. These synergistically positive effects have led to a high yield (~9.2%) of C_2 products with 51.9% C_2-selectivity and 17.7% CH_4 conversion at 850 °C. Note that the trend of the increased CH_4 conversion, C_2 selectivity and yield with temperature is consistent with our previous modeling work, but the experimental values are much lower than computational values [27]. One reason is that the modeling considers tubular plug-flow membrane reactors, which allows incremental addition of CO_2/O_2 into the CH_4 stream along the length of the membrane, thus mitigating side reactions (14)–(16).

A noteworthy observation is no CO detected in the effluent. This finding implies that there is no coking occurred in the above experiments and all the formed C_2H_6 is converted into C_2H_4 via simple thermal cracking (reaction 12)). Otherwise, CO_2 and O_2 would react with C to form CO. There is also no exothermic reverse water gas shift reaction because it is unfavorable at a temperature as high as 850 °C. We believe that both high operating temperature and the catalyst we used contribute to the "no-coking" behavior. In addition, we did not observe morphology change, see Fig. S2, or blackening of the catalyst after the OCM test, indicating the good stability of catalyst during OCM reaction.

To demonstrate the effect of the catalyst, the OCM performance of membrane reactor was also evaluated without catalyst under the same testing condition. As shown in Table S2, its OCM performance is much lower than that with catalyst. For example, at 850 °C, CH_4 conversion, C_2 products selectivity and yield are only 6.8%, 15.7% and 1.1%, respectively. This comparison demonstrates the importance of catalysts in the OCM conversion.

3.4. Thermodynamic analysis of OCM process

We also performed a theoretical analysis on the OCM process. From the mass balance of C, H and O, the permeated CO_2 and O_2 flux from flue

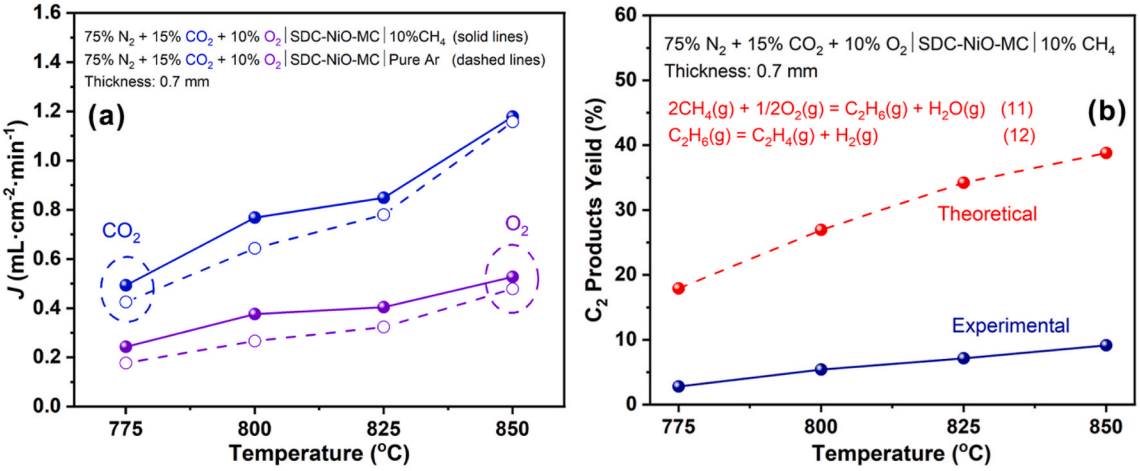

Fig. 9. (a) CO_2 and O_2 permeation fluxes calculated through SDC-NiO-MC membrane with 10% CH_4 as sweep gas and (b) comparison of measured C_2 products yield with theoretical values.

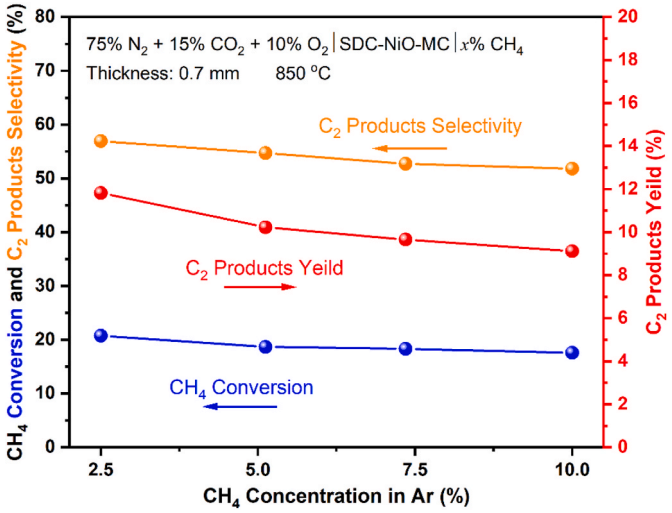

Fig. 10. Effect of CH_4 concentration on OCM performance of the SDC-NiO-MC membrane at 850 °C.

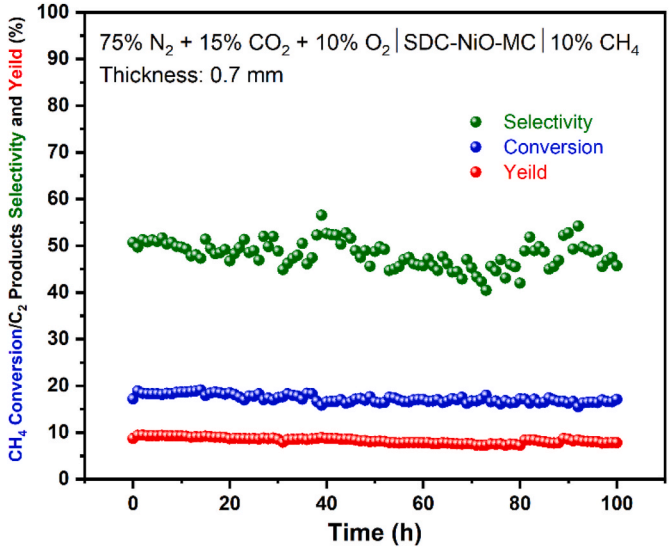

Fig. 11. Long-term stability of MECC-based OCM reactor under 10% CH_4 as sweep gas at 825 °C.

gas under 10%CH_4 as the sweep gas are calculated by:

$$\text{C}-\text{mass balance: } \dot{m}^{in}_{CH_4} + \dot{m}^{in}_{CO_2} = 2\dot{m}^{out}_{C_2H_4} + 2\dot{m}^{out}_{C_2H_6} + \dot{m}^{out}_{CO_2} \quad (17)$$

$$\text{H}-\text{mass balance: } 4\dot{m}^{in}_{CH_4} = 4\dot{m}^{out}_{C_2H_4} + 6\dot{m}^{out}_{C_2H_6} + 2\dot{m}^{out}_{H_2} + 2\dot{m}^{out}_{H_2O} \quad (18)$$

$$\text{O}-\text{mass balance: } 2\dot{m}^{in}_{O_2} + 2\dot{m}^{in}_{CO_2} = \dot{m}^{out}_{H_2O} + 2\dot{m}^{out}_{CO_2} \quad (19)$$

where $\dot{m}$ represents mass flow rate or flux. The CO_2 and O_2 flux densities calculated are specifically shown in Fig. 9a. Compared to the CO_2/O_2 flux with pure Ar sweep gas (Fig. 5a), the fluxes of CO_2/O_2 under 10% CH_4 are higher at any temperature, particularly at lower temperatures; this trending can be ascribed to the larger chemical potential gradient of O_2 and CO_2 across the membrane in the latter case. The theoretical C_2 products yield is also calculated out based on reactions (11) and (12), which are much higher than experimental values, see Fig. 9b. The large difference reflects a significant degree of side reactions (14)–(16), see Fig. S3, undertaken in the OCM process. To reduce the involvement of these side reactions, a tubular plug-flow membrane reactor configuration, in which CO_2/O_2 is incrementally added into the CH_4 stream along the axial length, will be beneficial, as modeling suggested [27].

The OCM performance was also evaluated as a function of CH_4 concentration at 850 °C; the results are shown in Fig. 10. Overall, there is no significant effect from the CH_4 concentration. Decreasing CH_4 concentration from 10 to 2.5% slightly increases C_2 selectivity but with a nearly constant CH_4 conversion. This is because, at lower CH_4 concentrations, there will be a higher percentage of CH_4 molecules to react with O_2 via reaction (11) forming C_2H_6 over the available reactive sites on the catalyst surface, leading to higher C_2-selectivity. In comparison, at higher CH_4 concentrations, those CH_4 molecules that do not have the access to catalyst surfaces for OCM reaction will react with O_2 via reaction (14)–(16), resulting in lowered C_2-selectivity. This trend is also in agreement with the theoretical calculations shown in Fig. S4. Nevertheless, in either case, the nearly constant CH_4 conversion reflects the membrane's capability to transform CH_4 into other chemicals (e.g. C_2H_6, CO_2, H_2O) via oxidative route. What determines the desirable C_2 selectivity is the catalyst. The presence of high concentrations of CO_2 in the reaction space helps suppress the side reactions (14)–(16). Note that ~12% C_2 yield (under 2.5%CH_4 at 850 °C) is still relatively lower than that reported by other larger co-fed reactors [17,18]. One of the main reasons is that the OCM performance in our work is restricted by small surface area (0.921 cm^2) of button-type membrane reactor. Ongoing research in the author's group is the development of tubular membrane

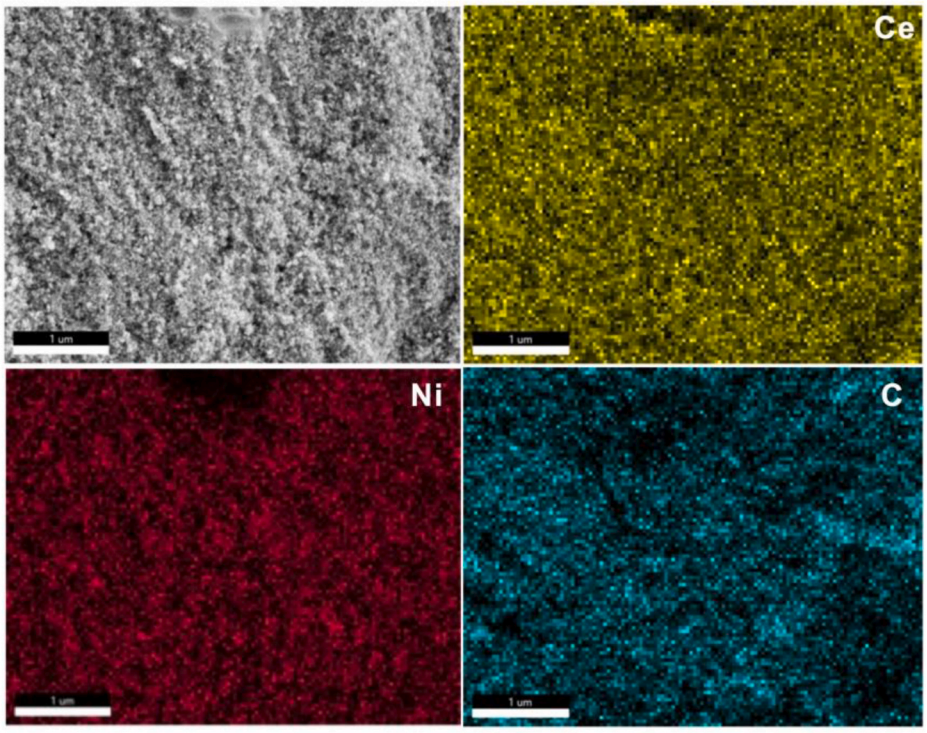

Fig. 12. Cross-sectional microstructure and elemental mapping of post long-term tested SDC-NiO-MC membrane of OCM reactor.

reactors with larger surface area, where a higher high-value product yield may be achieved. We will report the results when the data become available in the future.

3.5. Stability test of the membrane reactor

Stability is a very important criterion to evaluate any membrane reactor. Considering the instability of catalyst Mn–Na_2WO_4/SiO_2 after long-time exposure to high temperature (~830 °C) [31], the reaction temperature of long-term stability test was chosen to 825 °C. Fig. 11 shows CH_4 conversion, C_2 selectivity and C_2 yield are all stable during the ~100 h testing, suggesting a good stability of the NiO-SDC-MC membrane in both oxidizing and reducing and high CO_2 environment.

The cross-sectional views of the microstructure of post-test sample are shown in Fig. 12; the images indicate that the SDC-NiO-MC membrane is still microstructurally dense and contains well-connected SDC-NiO matrix and MC phases, demonstrating good robustness of the membrane.

4. Conclusions

In summary, the developed SDC-NiO-MC button-type membrane have been demonstrated with high CO_2/O_2 permeation flux densities using a mockup flue gas as the feed gas and Ar as the sweep gas. At 850 °C, the membrane exhibits a CO_2 and O_2 flux density of 1.16 and 0.48 $mL{\cdot}min^{-1}{\cdot}cm^{-2}$, respectively. The flux ratio between the permeated CO_2 and O_2 is found to be greater than 2:1, which is resulted from the predominant MECC and secondary MOCC transport mechanisms. By switching the sweep gas to CH_4-Ar and incorporating an OCM-specific catalyst, the same membrane reactor produces C_2 products (C_2H_6 and C_2H_4). At 2.5% CH_4, the reactor achieves >20% CH_4 conversion, ~57% C_2 selectivity, resulting in ~12% C_2 yield at 850 °C. The main side reactions affecting the C_2 selectivity are C_2H_6/C_2H_4 reoxidation and direct CH_4 oxidation. With a tubular plug-flow type of membrane, C_2 yield is expected to improve due to the incremental addition of CO_2/O_2 along the axial length of the membrane. The long-term test of the membrane reactor shows a stable performance for ~100 h at 825 °C. Overall, the SDC-NiO-MC CTM-based OCM reactor is a promising technology to upgrade CH_4 into high-value C_2 products with integrated CO_2 capture from flue gas and OCM process.

CRediT authorship contribution statement

Kangkang Zhang: performed experiments, Formal analysis, manuscript drafting. **Shichen Sun:** experimental assistance. **Kevin Huang:** Supervision, Conceptualization, finalizing manuscript.

Declaration of competing interest

The authors declare that they have no known competing financial interests or personal relationships that could have appeared to influence the work reported in this paper.

Data availability

Data will be made available on request.

Acknowledgement

We would like to thank US Department of Energy, Office of Fossil Energy, National Energy Technology Laboratory (Award # DE-FE-0031634), and National Science Foundation (Award # CBET-1924095) for supporting this work.

Appendix A. Supplementary data

Supplementary data to this article can be found online at https://doi.org/10.1016/j.memsci.2022.120915.

References

[1] H. Cheng, Future earth and sustainable developments, Innovation 1 (3) (2020), 100055, https://doi.org/10.1016/j.xinn.2020.100055.

[2] I. Sullivan, A. Goryachev, I.A. Digdaya, X. Li, H.A. Atwater, D.A. Vermaas, C. Xiang, Coupling electrochemical CO_2 conversion with CO_2 capture, Nat. Catalys. 4 (11) (2021) 952–958, https://doi.org/10.1038/s41929-021-00699-7.

[3] T.D. Burns, K.N. Pai, S.G. Subraveti, S.P. Collins, M. Krykunov, A. Rajendran, T. K. Woo, Prediction of MOF performance in vacuum swing adsorption systems for post-combustion CO_2 capture based on integrated molecular simulations, process optimizations, and machine learning Models, Environ. Sci. Technol. 54 (7) (2020) 4536–4544, https://doi.org/10.1021/acs.est.9b07407.

[4] T. Wilberforce, A.G. Olabi, E.T. Sayed, K. Elsaid, M.A. Abdelkareem, Progress in carbon capture technologies, Sci. Total Environ. 761 (2021), 143203, https://doi.org/10.1016/j.scitotenv.2020.143203.

[5] G.A. Mutch, L. Qu, G. Triantafyllou, W. Xing, M.-L. Fontaine, I.S. Metcalfe, Supported molten-salt membranes for carbon dioxide permeation, J. Mater. Chem. 7 (21) (2019) 12951–12973, https://doi.org/10.1039/c9ta01979k.

[6] N. Habib, Z. Shamair, N. Tara, A.-S. Nizami, F.H. Akhtar, N.M. Ahmad, M.A. Gilani, M.R. Bilad, A.L. Khan, Development of highly permeable and selective mixed matrix membranes based on Pebax®1657 and NOTT-300 for CO_2 capture, Separ. Purif. Technol. 234 (2020), https://doi.org/10.1016/j.seppur.2019.116101.

[7] Y. Ji, M. Zhang, K. Guan, J. Zhao, G. Liu, W. Jin, High-performance CO_2 capture through polymer-based ultrathin membranes, Adv. Funct. Mater. 29 (33) (2019), https://doi.org/10.1002/adfm.201900735.

[8] P. Zhang, J. Tong, K. Huang, X. Zhu, W. Yang, The current status of high temperature electrochemistry-based CO_2 transport membranes and reactors for direct CO_2 capture and conversion, Prog. Energy Combust. Sci. 82 (2021), 100888.

[9] N. Xu, X. Li, M.A. Franks, H. Zhao, K. Huang, Silver-molten carbonate composite as a new high-flux membrane for electrochemical separation of CO_2 from flue gas, J. Membr. Sci. 401–402 (2012) 190–194, https://doi.org/10.1016/j.memsci.2012.02.001.

[10] K. Zhang, S. Sun, N. Xu, K. Huang, H_2O-enhanced CO_2 transport through a proton conducting ceramic- molten carbonate dual-phase membrane, J. Membr. Sci. 650 (2022), https://doi.org/10.1016/j.memsci.2022.120421.

[11] L. Zhang, N. Xu, X. Li, S. Wang, K. Huang, W.H. Harris, W.K.S. Chiu, High CO_2 permeation flux enabled by highly interconnected three-dimensional ionic channels in selective CO_2 separation membranes, Energy Environ. Sci. 5 (8) (2012), https://doi.org/10.1039/c2ee22045h.

[12] C.A. Ortiz-Bravo, C.A. Chagas, F.S. Toniolo, Oxidative coupling of methane (OCM): an overview of the challenges and opportunities for developing new technologies, J. Nat. Gas Sci. Eng. 96 (2021), https://doi.org/10.1016/j.jngse.2021.104254.

[13] X. Meng, X. Cui, N.P. Rajan, L. Yu, D. Deng, X. Bao, Direct methane conversion under mild condition by thermo-, Electro-, or Photocatalysis, Chem 5 (9) (2019) 2296–2325, https://doi.org/10.1016/j.chempr.2019.05.008.

[14] B.L. Farrell, V.O. Igenegbai, S. Linic, A viewpoint on direct methane conversion to ethane and ethylene using oxidative coupling on solid catalysts, ACS Catal. 6 (7) (2016) 4340–4346, https://doi.org/10.1021/acscatal.6b01087.

[15] C. Karakaya, R.J. Kee, Progress in the direct catalytic conversion of methane to fuels and chemicals, Prog. Energy Combust. Sci. 55 (2016) 60–97, https://doi.org/10.1016/j.pecs.2016.04.003.

[16] D. Kiani, S. Sourav, I.E. Wachs, J. Baltrusaitis, Synthesis and molecular structure of model silica-supported tungsten oxide catalysts for oxidative coupling of methane (OCM), Catal. Sci. Technol. 10 (10) (2020) 3334–3345, https://doi.org/10.1039/d0cy00289e.

[17] A.M. Arinaga, M.C. Ziegelski, T.J. Marks, Alternative oxidants for the catalytic oxidative coupling of methane, Angew Chem. Int. Ed. Engl. 60 (19) (2021) 10502–10515, https://doi.org/10.1002/anie.202012862.

[18] D. Kwon, I. Yang, Y. Sim, J.-M. Ha, J.C. Jung, A K_2NiF_4-type $La_2Li_{0.5}Al_{0.5}O_4$ catalyst for the oxidative coupling of methane (OCM), Catal. Commun. 128 (2019), https://doi.org/10.1016/j.catcom.2019.05.009.

[19] C.A. Ortiz-Bravo, S.J.A. Figueroa, R. Portela, C.A. Chagas, M.A. Bañares, F. S. Toniolo, Elucidating the structure of the W and Mn sites on the Mn-Na_2WO_4/SiO_2 catalyst for the oxidative coupling of methane (OCM) at real reaction temperatures, J. Catal. (2021), https://doi.org/10.1016/j.jcat.2021.06.021.

[20] D. Kiani, S. Sourav, J. Baltrusaitis, I.E. Wachs, Oxidative coupling of methane (OCM) by SiO_2-supported tungsten oxide catalysts promoted with Mn and Na, ACS Catal. 9 (7) (2019) 5912–5928, https://doi.org/10.1021/acscatal.9b01585.

[21] O. Czuprat, T. Schiestel, H. Voss, J.r. Caro, Oxidative Coupling of Methane in a BCFZ Perovskite Hollow Fiber Membrane Reactor, 2010, pp. 10230–10236, https://doi.org/10.1021/ie100282g.

[22] N.H. Othman, Z. Wu, K. Li, An oxygen permeable membrane microreactor with an in-situ deposited $Bi_{1.5}Y_{0.3}Sm_{0.2}O_3$−catalyst for oxidative coupling of methane, J. Membr. Sci. 488 (2015) 182–193, https://doi.org/10.1016/j.memsci.2015.04.027.

[23] X. Tan, K. Li, Oxidative coupling of methane in a perovskite hollow-fiber membrane reactor, 45, 2006, pp. 142–149, https://doi.org/10.1021/ie0506320.

[24] E. Portillo, B. Alonso-Fariñas, F. Vega, M. Cano, B. Navarrete, Alternatives for oxygen-selective membrane systems and their integration into the oxy-fuel combustion process: a review, Separ. Purif. Technol. 229 (2019), https://doi.org/10.1016/j.seppur.2019.115708.

[25] W. Bai, J. Feng, C. Luo, P. Zhang, H. Wang, Y. Yang, Y. Zhao, H. Fan, A comprehensive review on oxygen transport membranes: development history, current status, and future directions, Int. J. Hydrogen Energy 46 (73) (2021) 36257–36290, https://doi.org/10.1016/j.ijhydene.2021.08.177.

[26] R. Kiebach, S. Pirou, L. Martinez Aguilera, A.B. Haugen, A. Kaiser, P.V. Hendriksen, M. Balaguer, J. García-Fayos, J.M. Serra, F. Schulze-Küppers, M. Christie, L. Fischer, W.A. Meulenberg, S. Baumann, A review on dual-phase oxygen transport membranes: from fundamentals to commercial deployment, J. Mater. Chem. 10 (5) (2022) 2152–2195, https://doi.org/10.1039/d1ta07898d.

[27] X. Li, K. Huang, N. Van Dam, X. Jin, Performance projection of a high-temperature CO_2 transport membrane reactor for combined CO_2 capture and methane-to-ethylene conversion, J. Electrochem. Soc. 169 (5) (2022), https://doi.org/10.1149/1945-7111/ac6ae7.

[28] T.W. Elkins, H.E. Hagelin-Weaver, Characterization of Mn–Na_2WO_4/SiO_2 and Mn–Na_2WO_4/MgO catalysts for the oxidative coupling of methane, Appl. Catal. Gen. 497 (2015) 96–106, https://doi.org/10.1016/j.apcata.2015.02.040.

[29] P. Zhang, J. Tong, K. Huang, A self-forming dual-phase membrane for high-temperature electrochemical CO_2 capture, J. Mater. Chem. 5 (25) (2017) 12769–12773, https://doi.org/10.1039/c7ta04096b.

[30] P. Zhang, J. Tong, K. Huang, Self-formed, mixed-conducting, triple-phase membrane for efficient CO_2/O_2 capture from flue gas and in situ dry-oxy methane reforming, ACS Sustain. Chem. Eng. 6 (11) (2018) 14162–14169, https://doi.org/10.1021/acssuschemeng.8b02776.

[31] W. Riedel, L. Thum, J. Möser, V. Fleischer, U. Simon, K. Siemensmeyer, A. Schnegg, R. Schomäcker, T. Risse, K.-P. Dinse, Magnetic properties of reduced and reoxidized Mn–Na_2WO_4/SiO_2: a catalyst for oxidative coupling of methane (OCM), J. Phys. Chem. C 122 (39) (2018) 22605–22614, https://doi.org/10.1021/acs.jpcc.8b07386.